

Self-consistent triaxial models

Jason L. Sanders^{1*} and N. Wyn Evans¹

¹*Institute of Astronomy, Madingley Road, Cambridge, CB3 0HA*

16 July 2015

ABSTRACT

We present self-consistent triaxial stellar systems that have analytic distribution functions (DFs) expressed in terms of the actions. These provide triaxial density profiles with cores or cusps at the centre. They are the first self-consistent triaxial models with analytic DFs suitable for modelling giant ellipticals and dark haloes. Specifically, we study triaxial models that reproduce the Hernquist profile from Williams & Evans (2015), as well as flattened isochrones of the form proposed by Binney (2014). We explore the kinematics and orbital structure of these models in some detail. The models typically become more radially anisotropic on moving outwards, have velocity ellipsoids aligned in Cartesian coordinates in the centre and aligned in spherical polar coordinates in the outer parts.

In projection, the ellipticity of the isophotes and the position angle of the major axis of our models generally changes with radius. So, a natural application is to elliptical galaxies that exhibit isophote twisting. As triaxial Stäckel models do not show isophote twists, our DFs are the first to generate mass density distributions that do exhibit this phenomenon, typically with a gradient of $\approx 10^\circ$ /effective radius, which is comparable to the data.

Triaxiality is a natural consequence of models that are susceptible to the radial orbit instability. We show how a family of spherical models with anisotropy profiles that transition from isotropic at the centre to radially anisotropic becomes unstable when the outer anisotropy is made sufficiently radial. Models with a larger outer anisotropy can be constructed but are found to be triaxial. We argue that the onset of the radial orbit instability can be identified with the transition point when adiabatic relaxation yields strongly triaxial rather than weakly spherical endpoints.

Key words: Galaxy, galaxies: kinematics and dynamics – methods: analytical, numerical.

1 INTRODUCTION

The case for the importance of triaxiality in galactic dynamics has a reasonably long history. Early studies by Binney (1978) and Illingworth (1977) proposed that giant elliptical galaxies are generically triaxial in shape and this hypothesis was reinforced by the N -body simulations of Aarseth & Binney (1978) that showed that aspherical initial conditions relaxed to triaxial distributions. More recently, triaxiality is believed to be a generic feature of so-called ‘slow rotator’ galaxies (Emsellem et al. 2007; Cappellari et al. 2007; Krajnović et al. 2011).

When tackling the data it becomes difficult to disentangle triaxiality from other effects, not least because we are only ever able to observe a projection of the distribution. However, even in projection, triaxiality can give rise to signature effects. In particular, a changing axis ratio of concentric ellipsoidal density contours gives rise to a twisting of the isophotes when viewed from a general angle. The slow rotators of the SAURON sample (Emsellem et al. 2007, those with $\lambda_R < 0.1$) show evidence of isophote twisting. In addition to inspecting a single galaxy for evidence of triaxiality,

statistics on the shapes of many galaxies yield important information. Using the assumption of random viewing angles and a wholly axisymmetric population one can recover the distribution of intrinsic axis ratios of a sample of galaxies. For instance, Tremblay & Merritt (1995) showed from a sample of 171 bright ellipticals that wholly oblate or prolate populations were ruled out and a triaxial population favoured. More recently, Weijmans et al. (2014) performed a similar procedure on the ATLAS-3D sample (Cappellari et al. 2011) and showed there were strong indications of triaxiality in the sample of slow rotators.

The recent SAURON and ATLAS-3D projects have complemented photometry with line-of-sight velocity distributions for samples of nearby galaxies. This additional information helps to unravel the internal dynamics, and hence the intrinsic shapes, of the galaxies. Binney (1985) proposed that rotation along the minor axis of projected elliptical density contours or instead kinematic misalignment (misalignment of the minor axis and the angular momentum vector) is indicative of triaxiality. Franx et al. (1991) inspected the statistics of minor-axis rotation for a sample of galaxies and found ≥ 35 per cent of their sample had kinematic misalignment. Weijmans et al. (2014) used kinematic misalignment to separate off potential triaxial candidates in their sample.

* E-mail: jls,nwe@ast.cam.ac.uk

So far our discussion of the evidence for triaxiality has been limited to the visible component of galaxies. The shapes of dark matter haloes remains an interesting open question. Many N -body simulators (Jing & Suto 2002; Bailin & Steinmetz 2005; Allgood et al. 2006) have demonstrated the range of possible triaxial dark matter haloes in cosmological simulations. However, the models relax to axisymmetry or sphericity when baryons are included in the simulations (Udry 1993; Dubinski 1994; Barnes & Hernquist 1996; Kazantzidis et al. 2004; Debattista et al. 2008) or when a central black hole forms (Merritt & Quinlan 1998). The case for triaxiality of the Milky Way’s dark matter halo is motivated by studies of the Sagittarius stream (Law & Majewski 2010; Vera-Ciro & Helmi 2013; Deg & Widrow 2013). However, several of these results are unsettling in that the short-axis of the dark matter halo lies in the disc plane (Debattista et al. 2013). Unhappily, the Sagittarius stream has proved hard to model, with no single fit able to explain the wealth of new data.

1.1 Dynamical models

Although there is considerable evidence for the presence of triaxiality in galaxies, the range of modelling tools available is severely limited. The two greatest developments in the understanding of triaxial stellar systems were the work of de Zeeuw (1985) on Stäckel or separable potentials and Schwarzschild (1979) on the construction of numerical dynamical equilibria. de Zeeuw (1985) showed that the only Stäckel potential in which the isodensity surfaces are concentric ellipsoids is the perfect ellipsoid and provided key insights into the classes of orbits that are expected to arise in generic triaxial potentials. Schwarzschild (1979) showed how a given triaxial density-potential pair could be self-consistently generated by linear superposition of numerically integrated orbits. Statler (1987) used this method to construct numerical dynamical models of de Zeeuw’s perfect ellipsoid and demonstrated that they generically produce kinematic misalignment when viewed in projection. However, as shown by Franx (1988), triaxial Stäckel models are unusual in that they are unable to produce isophote twisting. Schwarzschild’s method has proved useful in modelling external galaxies, but the only triaxial fit to an elliptical galaxy remains the work of van den Bosch et al. (2008) on NGC 4365 – though the related problem of modelling rotating triaxial bars has seen some progress (Zhao 1996; Häfner et al. 2000; Wang et al. 2013). Triaxial models have also been constructed using a made-to-measure approach (Syer & Tremaine 1996; Dehnen 2009), though here the only fits to data are for the Milky Way bar (Long et al. 2013; Portail et al. 2015).

An alternative approach to the construction of dynamical equilibria is through the use of integrals of motion. The Jeans theorem states that an equilibrium distribution function (DF) is solely a function of the integrals of motion. In spherical systems the classical integrals of the energy, E , and angular momentum, L , can be used to construct equilibrium models. For instance, Eddington inversion allows us to construct the isotropic $f(E)$ model given any radial density profile $\rho(r)$ and these calculations may incorporate anisotropy in a variety of ways (Osipkov 1979; Merritt 1985; Evans & An 2006; Binney & Tremaine 2008). Moving from sphericity to axisymmetry, it has long been realised that, in addition to the energy and a single-component of the angular momentum (e.g. the z -component L_z), numerically integrated orbits obey a third non-classical integral, I_3 (e.g., Ollongren 1962) and such a dependence in the DF seems necessary to reproduce the dynamics of the Milky Way and external galaxies (e.g., Binney 1976; Davies et al. 1983).

In general potentials, a global analytic third integral does not exist, but in axisymmetric Stäckel potentials this integral can be written down (e.g., Lynden-Bell 1962; de Zeeuw 1985). Similarly, in triaxial Stäckel potentials, we can find a second non-classical integral I_2 (a generalisation of a component of the angular momentum) to give three globally defined analytic integrals of motion. However, no analytic DFs based on the three integrals have ever been constructed for triaxial Stäckel models, with the exception of the very idealized case when the tube orbits are all infinitesimally thin (Hunter & de Zeeuw 1992). There are some DFs known for rotating triaxial stellar systems, though only for rather unrealistic density distributions such as homogeneous ellipsoids or polytropes (Freeman 1966; Vandervoort 1980).

1.2 Action-based distribution functions

As any function of the integrals of motion is also an integral of motion, we are free to take any choice of these functions as the basis for our DF. A natural choice is the action coordinates, \mathbf{J} . Along with the angle variables, they form a canonical set of coordinates. They possess the following advantages over the classical integrals: the range of each action is independent of the other actions, they are adiabatic invariants (crucial for the application in this paper) and they possess a physical meaning e.g. the ‘radial’ action J_r describes the extent of radial excursions (see Binney & Tremaine 2008, for more information). As the actions are adiabatic invariants, we are able to propose a form for the DF and iteratively converge to a self-consistent solution. However, in order to do this we must evaluate the properties of a given $f(\mathbf{J})$ model so we require routines to find \mathbf{J} given (\mathbf{x}, \mathbf{v}) . In spherical potentials the actions are given by $\mathbf{J} = (J_r, J_\phi, J_\theta) = (J_r, L_z, L - |L_z|)$. J_r can be calculated as a quadrature for any spherical potential. In recent years, several algorithms have been developed to estimate the actions in general potentials. Sanders (2012) proposed an algorithm where an axisymmetric potential was locally fitted by a Stäckel potential and then the actions estimated as those in the best-fitting Stäckel potential. A similar routine was presented by Binney (2012) who rewrote the equations for the actions in a Stäckel potential in such a way that they could be applied to a general potential. The accuracy of both of these approaches relied on the target potential being sufficiently close to a Stäckel potential but crucially only locally. Sanders & Binney (2015) built on the work of Binney (2012) by generalising the method to triaxial potentials. In addition to these approximate methods for finding the actions, Sanders & Binney (2014) presented a more accurate approach for general triaxial potentials that relied on the construction of a generating function from time samples of an orbit integration.

Given the tools now available for the calculation of actions, it is natural to begin constructing self-consistent action-based DFs. Binney (2014) demonstrated how the isochrone DF could be flattened to create a family of axisymmetric action-based models. More recently, both Posti et al. (2015) and Williams & Evans (2015) have proposed families of action-based distribution functions that reproduced the density profiles and kinematics of a range of spherical potentials. With the tools in hand to estimate actions in triaxial potentials, this paper makes the obvious next step of generalizing these models to triaxiality with the aim of producing models that are appropriate for the modelling of the triaxial structures discussed in the previous sections. We demonstrate how triaxial self-consistent models can be generated and inspect the properties of a few illustrative cases.

In Section 2, we detail all the pieces of machinery required

to construct self-consistent triaxial models. Some technical details are reserved for three appendices. In Section 3, we present triaxial versions of two recent action-based distribution functions in the literature. In Section 4, we discuss two novelties of the presented models: isophote twisting and the ability to explore the radial stability of the models. Finally, we discuss the importance of resonances and chaos for these models and other uses of the models in Section 5 and draw our conclusions in Section 6.

2 CONSTRUCTING A SELF-CONSISTENT TRIAXIAL MODEL

In order to find the self-consistent potential Φ for a given $f(\mathbf{J})$ we require a considerable amount of machinery. Here we will outline and review the various pieces of machinery required.

2.1 Review of the action estimation schemes

For the calculation of properties of a given $f(\mathbf{J})$, we require algorithms for the computation of \mathbf{J} from (\mathbf{x}, \mathbf{v}) given some general potential. Actions only exist for integrable potentials and chaos can play a significant role in many triaxial potentials (Merritt & Fridman 1996; Siopis & Kandrup 2000). We will assume in what follows that all orbits can be labelled by an action (or some approximate action) and defer discussion of the presence of resonances and chaos to section 5.

We will use two algorithms for the computation of actions. The first is the triaxial Stäckel fudge method introduced in Sanders & Binney (2015) and is appropriate for the rapid generation of models. The second is a slower but more accurate method using the generating function from a analytic set of angle-actions to the target calculated from orbit integration. This second method was detailed in Sanders & Binney (2014) and will be useful for checking the results of our calculations using the Stäckel fudge. Here, we give an outline of the first of these methods and detail any alterations made for the current application. The second method is detailed in Appendix C where a cross-check of our calculations is presented.

2.2 Triaxial Stäckel fudge

Sanders & Binney (2015) introduced an algorithm for rapidly estimating the actions in a general triaxial potential. It built on the work of Binney (2012) and operates by assuming the target potential is sufficiently close to a Stäckel potential over the region a given orbit explores.

The Hamilton-Jacobi equations are separable in a Stäckel potential such that the actions can be expressed as 1D quadratures. The canonical coordinates in which the equations separate are (τ, p_τ) where τ are ellipsoidal coordinates (λ, μ, ν) given by the roots of

$$\frac{x^2}{\tau + \alpha} + \frac{y^2}{\tau + \beta} + \frac{z^2}{\tau + \gamma} = 1. \quad (1)$$

Here, (x, y, z) are Cartesian coordinates and α, β, γ are parameters that describe the confocal coordinate system. We impose $\alpha < \beta < \gamma$ such that x is the long axis and z the short axis.

The most general Stäckel potential, Φ_S , can be expressed as

$$\Phi_S(\lambda, \mu, \nu) = \sum_{(\lambda\mu\nu)} \frac{f(\lambda)}{(\lambda - \mu)(\nu - \lambda)}, \quad (2)$$

where $(\lambda\mu\nu)$ denotes cyclic permutations of the three variables. Φ_S is composed of a single function of one variable, $f(\tau)$. The equations of motion can be written as

$$2(\tau + \alpha)(\tau + \beta)(\tau + \gamma)p_\tau^2 = \tau^2 E - \tau a + b + f(\tau) \quad (3)$$

where E is the energy and a and b are separation constants. p_τ is solely a function of τ such that the actions are given by 1D quadratures

$$J_\tau = \frac{2}{\pi} \int_{\tau_-}^{\tau_+} d\tau |p_\tau(\tau)|. \quad (4)$$

(τ_-, τ_+) are the roots of the right hand side of equation (3). Note that as in Sanders & Binney (2015) we have defined a full oscillation in τ to be two full oscillations from τ_- to τ_+ and back again. This gives twice the true radial action for loop orbits but means orbits continuously fill action space (Binney & Spergel 1984).

Given a general triaxial potential, we define the quantities

$$\begin{aligned} \chi_\lambda(\lambda, \mu, \nu) &\equiv (\lambda - \mu)(\nu - \lambda)\Phi(\lambda, \mu, \nu), \\ \chi_\mu(\lambda, \mu, \nu) &\equiv (\mu - \nu)(\lambda - \mu)\Phi(\lambda, \mu, \nu), \\ \chi_\nu(\lambda, \mu, \nu) &\equiv (\nu - \lambda)(\mu - \nu)\Phi(\lambda, \mu, \nu). \end{aligned} \quad (5)$$

If Φ were a Stäckel potential, these quantities would be given by, for instance,

$$\chi_\lambda(\lambda, \mu, \nu) = f(\lambda) - \lambda \frac{f(\mu) - f(\nu)}{\mu - \nu} + \frac{\nu f(\mu) - \mu f(\nu)}{\mu - \nu}. \quad (6)$$

Therefore, for a general potential, we can write

$$f(\tau) \approx \chi_\tau(\lambda, \mu, \nu) + C_\tau \tau + D_\tau, \quad (7)$$

where C_τ and D_τ are constants provided we always evaluate χ_τ with two of the ellipsoidal coordinates fixed. For instance, we always evaluate χ_λ at fixed μ and ν .

When we substitute these expressions into equation (3), we find

$$2(\tau + \alpha)(\tau + \beta)(\tau + \gamma)p_\tau^2 = \tau^2 E - \tau A_\tau + B_\tau + \chi_\tau(\lambda, \mu, \nu). \quad (8)$$

For each τ coordinate, there are two new integrals of motion given by $A_\tau = a - C_\tau$ and $B_\tau = b + D_\tau$. Using a single 6D coordinate and a choice of coordinate system gives us a single constraint on a combination of A_τ B_τ . Due to the separability of the Hamilton-Jacobi equation, the partial derivative of the Hamiltonian with respect to any of the ellipsoidal coordinates is zero for a true Stäckel potential. Setting it equal to zero for a general potential gives a further constraint on A_τ and B_τ allowing us to solve for these integrals given only a single (\mathbf{x}, \mathbf{v}) coordinate. We have therefore produced approximate $p_\tau(\tau)$ equations of motion which may be integrated to estimate the actions.

In the above algorithm, the only parameters we can control are α and β which determine the location of the foci. We set $\gamma = -1$ without any consequences. These are chosen on an orbit-by-orbit basis so we are free to change them every time we require another action. We give details of the method employed to do this in Appendix A.

2.3 Adiabatic relaxation

A DF must obey the collisionless Boltzmann equation. For some applications such as the stellar halo, we may consider the DF of a tracer population with negligible mass that lives in the potential generated by a more dominant component. However, when treating massive components of galaxies, it is preferable for the model to

self-consistently generate its own potential. This poses a problem for action-based DFs. In order to find the density and the potential of an action-based DF, we must know the potential in order to calculate the actions. Therefore, the models must be constructed iteratively.

As the actions are adiabatic invariants, the form of the DF does not change under slow changes of the potential. We therefore pose an initial guess of the potential Φ_0 and find the potential Φ_1 of the DF in Φ_0 . We repeat this procedure with Φ_0 replaced by Φ_1 until the difference between the two potentials is less than \sim one per cent everywhere. This procedure is not guaranteed to converge if Φ_0 is very different from Φ_1 . To aid with convergence Binney (2014) used a linear combination of Φ_0 and Φ_1 as the next trial potential. We did not adopt that procedure here but found our models converged within ~ 8 iterations.

2.4 Multipole expansion

At each stage in the iterative procedure, we require the potential calculated from the density. Here, we are working with general triaxial mass distributions so we evaluate the potential using a multipole expansion (Binney & Tremaine 2008). We discuss the details of this in Appendix B.

2.5 Tests

The code was tested by reproducing spherical versions of the models detailed in the next section allowing for triaxiality and comparing to the models constructed by limiting the models to sphericity (i.e. using only $l = 0$ and $m = 0$ terms in the multipole expansion and calculating the actions in a spherical potential). Tests of the multipole expansion code are given in Appendix B. The action-finding code has been tested in Sanders & Binney (2015) and it was found that the actions were accurate to $\lesssim 10$ per cent for a typical box orbit and $\lesssim 5$ per cent for a typical loop orbit in a triaxial NFW potential. A comparison of the density calculation with two different action estimation approaches is presented in Appendix C.

3 ACTION-BASED MODELS

Due to the limited number of cases for which analytic self-consistent action-based DFs can be computed the study of action-based DFs has been fairly limited. In this section, we give details of several recent models which will be of use in constructing triaxial models. We consider DFs that are functions of the absolute values of the actions. Therefore, these models do not have a streaming velocity. This is not a necessary requirement for the models but it simplifies their construction. In all formulae, M is the mass of the model and \mathcal{N} is the normalization given by

$$\begin{aligned} \mathcal{N} &= M^{-1} (2\pi)^3 \int d^3 \mathbf{J} f(\mathbf{J}) \\ &= M^{-1} (2\pi)^3 \mathcal{F} \int_0^\infty dJ_r \int_0^\infty dJ_\phi \int_0^\infty dJ_\theta f(\mathbf{J}). \end{aligned} \quad (9)$$

The definition of the actions in the triaxial case (i.e. the radial action for the loop orbits is multiplied by two) means the integral includes loop orbits rotating in both senses so $\mathcal{F} = 1$ but in the spherical case we must multiply the integral by a factor of $\mathcal{F} = 2$ to include orbits rotating both clockwise and anticlockwise. We introduce a change of variables $s_i = J_i/(J_0 + J_i)$ to map the infinite limit to $(0, 1)$ and calculate the integral numerically using the Divonne

routine in the CUBA package (Hahn 2005) (all integrals over the DF are performed with this package). Additionally in the triaxial case we evaluate the distribution function as $f(\frac{1}{2}J_r, J_\phi, J_\theta)$ such that we correctly map onto the spherical case.

Sanders & Binney (2015) inspected a simple DF given by

$$f_{\text{SB}}(\mathbf{J}) = M\mathcal{N}(J_0 + \mathcal{L}(\mathbf{J}))^p, \quad (10)$$

where

$$\mathcal{L}(\mathbf{J}) = J_r + a_\phi |J_\phi| + a_\theta |J_\theta|. \quad (11)$$

Here, the coefficients a_i are constants and J_0 is a scale action. The models were evaluated in a fixed Navarro-Frenk-White potential and so were not self-consistent. They have a density core and density fall-off like r^{-3} and the coefficients controlled the kinematics. Two models were studied and it was demonstrated that the Jeans equation was satisfied to good accuracy. These models are simple, but lack flexibility. Here we examine two other models from the literature which we will study further with our new machinery.

3.1 Williams & Evans models

Williams & Evans (2015) proposed a family of action-based models with double power-law density profiles of the form

$$\rho \propto r^a (r_0 + r)^{(b-a)} \quad (12)$$

and tunable anisotropy profiles. The models built on the work of Williams et al. (2014) who demonstrated that in scale-free spherical potentials ($\Phi \propto r^\epsilon$), the Hamiltonian is well approximated by a homogeneous function of degree one in the actions i.e. $H(\mathbf{J}) \propto (L + D_{\text{WEB}} J_r)^\zeta$ where $\zeta = 2\epsilon/(\epsilon + 2)$. D_{WEB} is a coefficient that can be calculated by considering the limiting cases $J_r = 0$ and $L = 0$. Adjusting D_{WEB} away from the isotropic value produces models with constant non-zero anisotropy.

For a double power law in the density, the potential in the near and far field is well approximated by a scale-free power law such that an appropriate isotropic DF can be constructed by stitching together two scale-free $H(\mathbf{J})$ as

$$f_{\text{WE}}(\mathbf{J}) = \mathcal{N} M \frac{T(|\mathbf{J}|) \mathcal{L}(\mathbf{J})^{-\delta}}{[J_0^2 + \mathcal{L}(\mathbf{J})^2]^{(\eta-\delta)/2}}, \quad (13)$$

where

$$\mathcal{L}(\mathbf{J}) = L + D(|\mathbf{J}|) J_r. \quad (14)$$

Here, J_0 is a scale action related approximately to the scale radius r_0 of the model as $J_0 = \sqrt{GM} r_0$ and $\delta = (6 - a)/(4 - a)$ and $\eta = 2b - 3$. Both $D(|\mathbf{J}|)$ and $T(|\mathbf{J}|)$ are transit functions of the form

$$\mathcal{T}(|\mathbf{J}|) = \frac{\mathcal{T}_0 + \mathcal{T}_1 |\mathbf{J}|/J_\tau}{1 + |\mathbf{J}|/J_\tau}, \quad (15)$$

where $|\mathbf{J}| = \sqrt{J_r^2 + L^2}$. $\mathcal{T}(|\mathbf{J}|)$ evolves from \mathcal{T}_0 to \mathcal{T}_1 over a scale J_τ . $T(|\mathbf{J}|)$ controls the weight of the near-field part of the model relative to the far-field part. It acts to adjust the location of the break-radius in the density profile. $D(|\mathbf{J}|)$ controls the anisotropy of the model. Note that the scale-action is summed in quadrature with \mathcal{L} . This was found by Williams & Evans (2015) to produce better fits to the curvature of the density profile around the break radius. The model presented by Williams & Evans (2015) is very similar to that presented by Posti et al. (2015). However, the model of Williams & Evans (2015) is more flexible in the range of density profiles and kinematics that can be fitted so we adopt it here.

In the spherical case the actions J_ϕ and J_θ are combined into $L = |J_\phi| + |J_\theta|$ so $J_\theta = L - |J_\phi|$. To generalize these models beyond sphericity, we set

$$\mathcal{L} = D(|\mathbf{J}|)|J_r| + |J_\phi| + |J_\theta|/q_z. \quad (16)$$

q_z acts to flatten the model in the z -direction. Some combinations of parameters will produce axisymmetric models, whilst others will be triaxial, but there is no way of finding the symmetry of the model without a full calculation.

3.1.1 Example model

As a demonstration of the methodology, we will construct triaxial analogues of the [Hernquist \(1990\)](#) profile using equation (13). We refer to these as WEH models, as they use the ansatz introduced by [Williams & Evans \(2015\)](#).

A spherical Hernquist profile has the density-potential pair

$$\rho_H(r) = \frac{M}{2\pi} \frac{1}{r(r_0 + r)^3}, \quad (17)$$

$$\Phi_H(r) = -\frac{GM}{r + r_0}.$$

We set $G = M = r_0 = 1$. To construct an appropriate action-based model for this profile, we take the parameters from [Williams & Evans \(2015\)](#) as a starting point. They find an isotropic Hernquist profile is given by $\delta = 5/3$, $\eta = 5$, $D_0 = D_{\text{WEB}} = 1.814$, $D_1 = 1$, $T_0 = 0.378$, $T_1 = 1$, $J_0 = J_T = 1$ and $J_D = 0.41$. We then introduce a flattening $q_z = 0.4$. This simple alteration produces a model that is oblate in the far-field but weakly prolate in the centre. As our action-finding algorithm is not designed to find the actions in prolate cases, these results are perhaps not to be completely trusted. To encourage the model to be oblate at the centre, we increased the central radial anisotropy by decreasing D_0 . As noted in [Williams & Evans \(2015\)](#) when altering D_i , T_i must be adjusted accordingly to retain the required density profile as

$$T_0 \rightarrow T_0 \left(\frac{1 + D_{\text{WEB}}}{1 + D_0} \right)^{-\delta} \quad (18)$$

$$T_1 \rightarrow T_1 \left(\frac{2}{1 + D_1} \right)^{-\eta}.$$

For $D_0 = 1$, the model is triaxial at the centre (we will discuss under what conditions the models become triaxial later). We use as our initial potential guess a Hernquist profile flattened in the potential by $b/a = 0.98$ and $c/a = 0.95$. In Fig. 1, we show the convergence of the $D_0 = 1$ model towards self-consistency. Note also that at each radial point, there is a spread of points corresponding to a range of spherical polar angles.

In Figure 2, we plot the density contours of the model in the (x, y) plane and (x, z) plane along with the axis ratios of the best-fitting ellipses to the density and potential contours. b/a is the ratio in the (x, y) plane, whilst c/a is the ratio in the (x, z) plane (note here we could simply use the ratio of the intercepts of the coordinate axes, but as the models exhibit a slight peanut shape this gives a false impression of the shape of the contours). We can see that the model is triaxial at the centre with central values $(b/a)_\rho(r = r_0/10) \approx 0.7$ and $(c/a)_\rho(r = r_0/10) \approx 0.4$. For $r > 10r_0$, the potential is much more spherical, whilst the density is still flattened. At these large radii, there is little mass. As the total mass is finite, the behaviour at large radii mimics that of a tracer population in a monopole potential. The density contours in (x, z) are not elliptically shaped, but take on a slight peanut shape. [Emsellem et al. \(2011\)](#) shows that the slow rotators in the

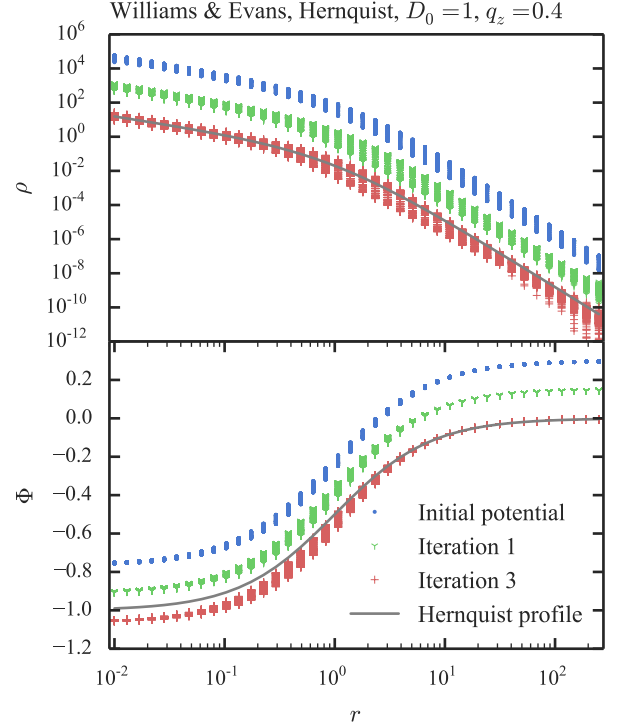


Figure 1. Convergence and final profiles of a triaxial WEH model: the top panel shows three iterations of the density calculation at arbitrary multiplicative offsets for visibility (the final iteration has no offset) and the bottom panel shows the corresponding potentials with arbitrary additive offsets. The blue dots show the calculation in the initial Hernquist potential (shown in grey), the green down-facing carets show the first iteration, red crosses the third and final iteration. Note we show the density calculated at several (ϕ, θ) values for each spherical radius r to give an indication of the triaxiality of the model. The positions are in units of r_0 , the density in units of M/r_0^3 and the potential in units of GM/r_0 .

ATLAS-3D sample (i.e. possible triaxial galaxies) have a boxiness ratio a_4/a consistent with pure elliptical or slightly boxy. Those that have slightly discy contours appear to have a kinematically decoupled core. It is therefore interesting that peanut-shaped distributions arise in the models (and also in the models of [Schwarzschild \(1979\)](#)), but not in nature. However, we should note that the degree of triaxiality presented here is larger than many galaxies are believed to have. Also, we will see later that in projection these models look elliptical.

In Figure 3, we show the density profile along a radial ray at the spherical polar angles $\phi = \pi/4$ and $\theta = \pi/4$ decomposed in terms of the orbit classification. We see that in the centre of the model, the majority of the density is contributed by the box orbits whilst in the outskirts the long and short axis loops contribute equally. The orbits are classified based on their limits in the Stäckel fudge scheme as described in [Sanders & Binney \(2015\)](#). A small fraction of orbits have boundaries that do not correspond to any orbital class in a Stäckel potential so we label them as approximately box, short-axis loop or long-axis loop depending on the relative magnitude of their actions. Our orbit classification method artificially imposes regularity on the orbital contribution to the model as some orbits will be chaotic but incorrectly given a regular label. There exist several methods for ascertaining whether an orbit is regular or chaotic (e.g.

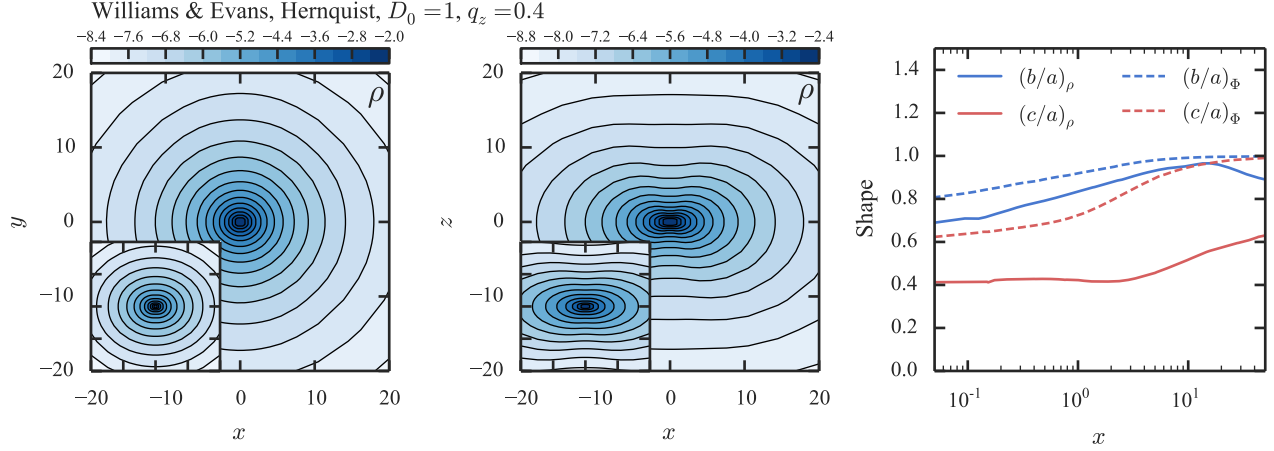


Figure 2. Density and shape of the triaxial WEH model: the left panel shows a slice of the density in the (x, y) plane and the middle panel shows the equivalent in the (x, z) plane. The blue colours indicate the base 10 logarithm of the density relative to the central value. The insets show zoom-ins for $|x| < 1, |y| < 1$ and $|x| < 1, |z| < 1$. In the right-hand panel, we show the axis ratios of the fitted ellipses in these two planes with solid lines $[b/a]$ corresponding to (x, y) and c/a (x, z) . The dashed lines show the equivalent for the potential. The positions are in units of r_0 and the density is in units of M/r_0^3 .

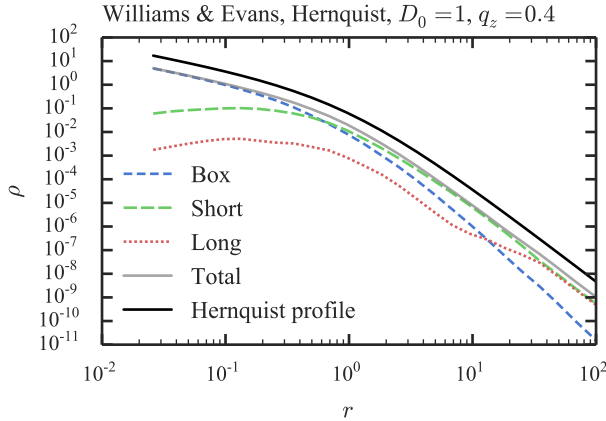


Figure 3. Contributions to the density in the triaxial WEH model along a radial ray with $\phi = \frac{\pi}{4}, \theta = \frac{\pi}{4}$. The boxes contribute most at the centre, whilst the loop orbits contribute equally in the outskirts where the potential is roughly spherical. Also shown is a true Hernquist profile offset by a factor of three for visibility. The positions are in units of r_0 and the density is in units of M/r_0 .

Lyapunov exponents – see [Vasiliev \(2013a\)](#) for a nice summary or the small alignment index [SALI] [Skokos et al. \(2003\)](#) that was applied recently to characterise the orbits in an axisymmetric galactic potential by [Zotos \(2014\)](#)) but these require long orbit integration. It seems for non-rotating galactic potentials of interest the majority of weight is on orbits that appear regular over a Hubble time (see Section 5 for more discussion) such that our orbital decomposition is meaningful.

In Figure 4, we show the velocity dispersions in the (x, y) and (x, z) planes. σ_{xx}^2 and σ_{yy}^2 produce approximately elliptical contours whilst σ_{zz}^2 produces a narrow waisted distribution in the (x, z) plane with the dispersion falling off much more slowly along the z axis. We also plot the velocity ellipses in the same two planes. Clearly the velocity ellipses are very radial for $z > 0$. In the (x, z)

plane, the ellipses are near radially-aligned for most of the explored space. At large radii, the ellipses become more radially aligned and at small radii they appear to become aligned with the Cartesian coordinates. In the (x, y) plane, we have a similar situation but the ellipses are near circular so any alignment of the ellipses in this plane is subtle. This configuration is seen in models with Stäckel potentials as the velocity ellipsoids are aligned with the confocal ellipsoidal coordinate system. Fig. 3 shows that at the centre of the model the box orbits dominate so the coordinate system is naturally aligned with Cartesian coordinates whilst beyond the scale radius loop orbits become more significant and the velocity ellipses naturally become more spherically aligned. Although we have used a Stäckel-based approach to estimate the actions, we have allowed the focal distances of the coordinate system to be a function of energy so we believe that this configuration is not a consequence of our calculation but a genuine feature of the models

3.2 Binney’s flattened isochrones

The spherical isochrone density-potential pair is given by

$$\begin{aligned} \rho_1(r) &= \frac{M}{4\pi} \frac{3(r_0 + r_a)r_a^2 - r^2(r_0 + 3r_a)}{r_a^3(r_0 + r_a)^3}, \\ \Phi_1(r) &= -\frac{GM}{r_0 + r_a}, \end{aligned} \quad (19)$$

where $r_a = \sqrt{r_0^2 + r^2}$ ([Binney & Tremaine 2008](#)). The isochrone density profile has a constant core and falls off as r^{-4} at large radii. The isochrone potential is convenient as it is the most general potential in which the actions can be analytically calculated ([Evans et al. 1990](#)). The Hamiltonian as a function of the actions is

$$H_1(\mathbf{J}) = -\frac{(GM)^2}{2[J_r + \frac{1}{2}(L + \sqrt{L^2 + 4GM r_0})]^2}. \quad (20)$$

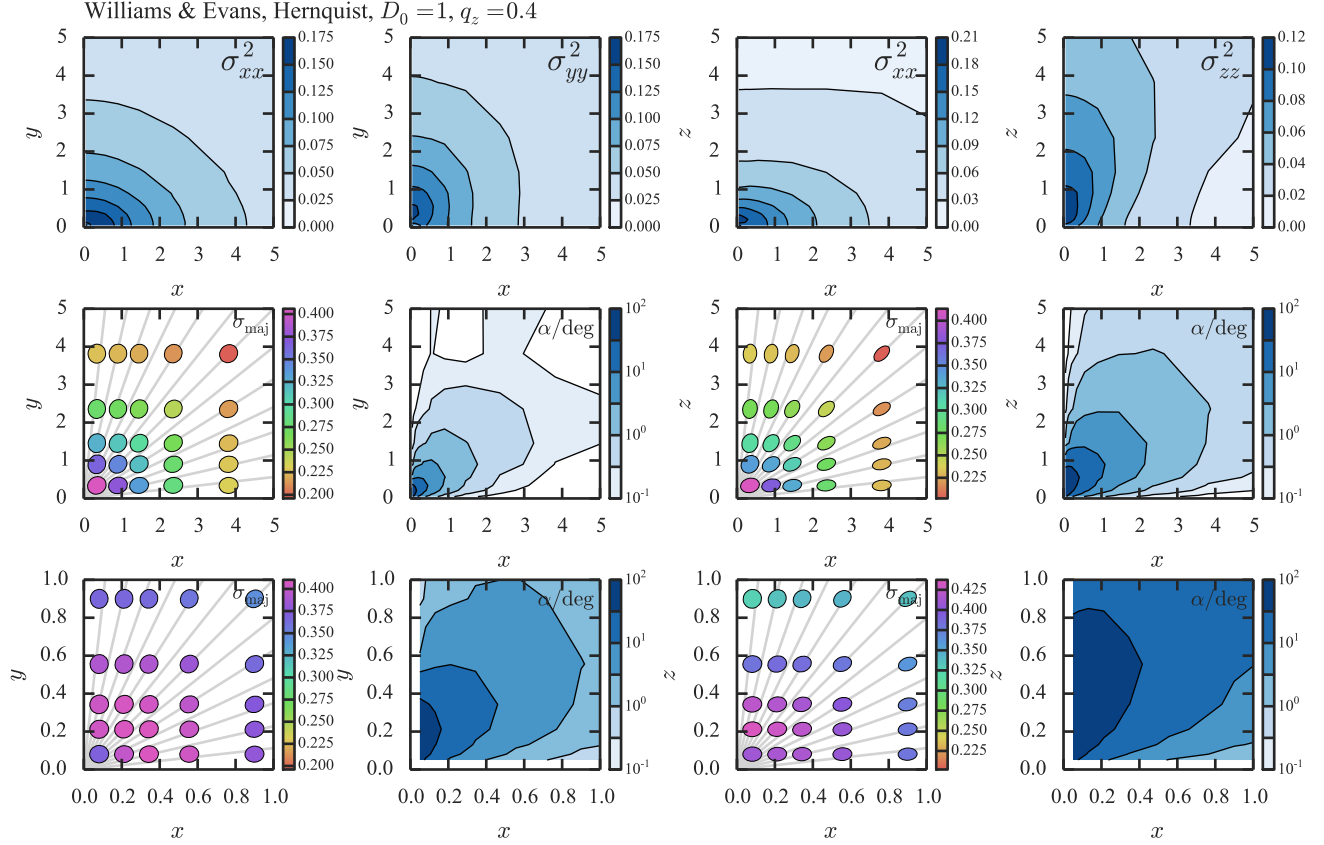


Figure 4. Velocity dispersions and ellipses of triaxial WEH model: in the top row the first panel shows σ_{xx}^2 in the (x, y) plane, the second panel shows σ_{yy}^2 in the (x, y) plane, the third panel shows σ_{xz}^2 in the (x, z) plane and the fourth panel shows σ_{zz}^2 in the (x, z) plane. In the second row, the first panel shows the velocity ellipses in the (x, y) plane, the second panel shows the tilt with respect to the radial direction (drawn in light grey in the first panel) in the (x, y) plane, the third panel shows the velocity ellipses in the (x, z) plane and the fourth panel shows the tilt with respect to the radial in the (x, z) plane. The colours show the magnitude of the velocity dispersion along the major axis of each ellipse and only the shape of the ellipse is important. The sizes of the ellipses are arbitrary. The bottom row shows a zoom-in of the second row. The positions are in units of r_0 and the dispersions are in units of \sqrt{GM}/r_0 .

Hénon (1960) demonstrated via Eddington inversion that the isotropic distribution function is given by

$$f_1(H_1) = \frac{\mathcal{N}}{\sqrt{2}(2\pi)^3(GMr_0)^{3/2}} \frac{\sqrt{\mathcal{H}}}{[2(1-\mathcal{H})]^4} \left[27 - 66\mathcal{H} + 320\mathcal{H}^2 - 240\mathcal{H}^3 + 64\mathcal{H}^4 + 3(16\mathcal{H}^2 + 28\mathcal{H} - 9) \frac{\sin^{-1} \sqrt{\mathcal{H}}}{\sqrt{\mathcal{H}(1-\mathcal{H})}} \right], \quad (21)$$

where

$$\mathcal{H} = -\frac{H_1 r_0}{GM}. \quad (22)$$

Note here $\mathcal{N} = 1$ but we retain it as it is necessary when adjusting the DF. Binney (2014) proposed a scheme to flatten these models such that axisymmetric analogues of the isochrone could be constructed. The density of the model in planes of constant energy is adjusted by scaling each of the actions by α_i . The new model is given by

$$f_B(\mathbf{J}) = \alpha_r \alpha_\phi \alpha_\theta f_1(\alpha_r J_r, \alpha_\phi J_\phi, \alpha_\theta J_\theta). \quad (23)$$

In order to retain the spherically-averaged density profile of the isochrone, the α_i are not independent. We are free to choose two

constants $\alpha_{\phi 0}$ and $\alpha_{\theta 0}$. The coefficients are given by

$$\begin{aligned} \alpha_r(\bar{\mathbf{J}}) &= (1 - \psi)\alpha_0 + \psi\alpha_{r0}, \\ \alpha_\phi(\bar{\mathbf{J}}) &= (1 - \psi)\alpha_0 + \psi\alpha_{\phi 0}, \\ \alpha_\theta(\bar{\mathbf{J}}) &= \alpha_{\theta 0}, \end{aligned} \quad (24)$$

where

$$\begin{aligned} \alpha_0(\bar{\mathbf{J}}) &= 1 - \frac{\Omega_L}{\Omega_L + \Omega_r}(\alpha_{\theta 0} - 1), \\ \alpha_{r0}(\bar{\mathbf{J}}) &= 1 - \frac{\Omega_L}{\Omega_r}(\alpha_{\phi 0} + \alpha_{\theta 0} - 2), \\ \psi(\bar{\mathbf{J}}) &= \tanh(\bar{\mathbf{J}}/\sqrt{GM}r_0). \end{aligned} \quad (25)$$

In these expressions, the frequencies, Ω_i , are evaluated in the spherical isochrone potential at the actions $\bar{\mathbf{J}} = (\bar{J}, \bar{J}, \bar{J})$ which is the barycentre of a plane of constant energy given by¹

$$\bar{J} = \frac{1}{3} \left(\frac{2GM}{\sqrt{-2E}} - \sqrt{\frac{(GM)^2}{-2E} + 3GM}r_0 \right). \quad (26)$$

¹ Note there is a typo in equation (11) of Binney (2014) such that the expression inside the square root should read $\frac{(GM)^2}{-2E} + 3GM}r_0$, not $\frac{(GM)^2}{-2E} - 3GM}r_0$.

In this equation E is evaluated using $H(J)$ for the spherical isochrone. Expressions for the frequencies are given in Binney & Tremaine (2008). The linear combination in equation (24) was introduced by Binney (2014) to produce models that did not become prolate at the centre. In this way α_r tends to α_ϕ at low barycentric action.

3.2.1 Example model

We now construct a triaxial generalization of one of these models. In order to induce triaxiality, we require $\alpha_{\theta 0} > 1$ such that the model is flattened in the z direction and $\alpha_{r0} < \alpha_{\phi 0}$ such that the model is radially biased. However, we also require $\alpha_{\phi 0} + \alpha_{\theta 0} < 3$ such that $\alpha_{r0} > 0$ everywhere.

We initially tried the $\alpha_{\phi 0} = 1, \alpha_{\theta 0} = 1.4$ model presented in Binney (2014) but this produced a near-axisymmetric model. We instead opted for $\alpha_{\theta 0} = 1.3$ and $\alpha_{\phi 0} = 1.6$ and we set $G = M = r_0 = 1$. This produced a weakly triaxial model. In Figure 5, we plot the density contours of the model in the (x, y) plane and (x, z) plane along with the axis ratios of the best-fitting ellipses to the density and potential contours. We can see that model is triaxial at the centre with $(b/a)_\rho(r = r_0/10) \approx 0.8$ and $(c/a)_\rho(r = r_0/10) \approx 0.7$. For $r > 10r_0$ the potential is tending towards spherical whilst the density is still flattened. We see the strong core in the density contours of the model and the slight boxy shape of the density contours in the (x, z) plane.

In Figure 6, we show the density profile along a radial line at the spherical polar angles $\phi = \frac{\pi}{4}$ and $\theta = \frac{\pi}{4}$ decomposed in terms of the orbit classification. At the centre, nearly all the density is contributed by the box orbits. The contribution to the density from the loop orbits turns over around $r = r_0$ due the harmonic core of the potential. For $r_0 < r < 3r_0$ the short-axis loop orbits and the box orbits are contributing equally whilst beyond $r = 3r_0$ the long-axis loop orbits dominate. In the outskirts, the long-axis loops contribute most with very weak contributions from the box orbits and the short-axis loops. This combination is clearly necessary to produce the observed triaxial shape in the outskirts. It is interesting to note the similarities and differences from the Hernquist model. In both cases the density of box orbits outweighs the loop orbits by two orders of magnitude. However, for the isochrone model the long and short axis loops contribute equally whilst for the Hernquist model the long axis loop orbit contributes over an order of magnitude less density than the short axis loop orbits. At large radii the box orbits contribute weakly in both cases with the loop orbits contributing most to the density. However, in the Hernquist model the short and long axis loop orbits are contributing equally at large radii whilst in the isochrone model the long-axis loop orbits are dominating the density. Note that in this case, unlike with the WEH model, the total density profile differs from an isochrone profile. The models will only exactly match for small $|\alpha_i - 1|$ which is not satisfied for this model as $\alpha_R \approx 3 - \alpha_\phi - \alpha_z \approx 0.1$. However, the inner and outer slopes match well.

In Figure 7, we show the velocity dispersions in the (x, y) and (x, z) planes. σ_{xx}^2 and σ_{yy}^2 produce approximately elliptical contours within $r \approx 2r_0$ as with the Hernquist case. However, the velocity dispersions at the centre do not rise nearly as steeply as in the Hernquist case. Interestingly, the σ_{xx}^2 contours break from ellipticity for $y > 3r_0$ as the outermost contour shown has a positive curvature. Also σ_{yy}^2 seems to have a narrow waisted distribution for $x \gtrsim 3r_0$. As in the Hernquist case, σ_{zz}^2 produces a narrow-waisted distribution in the (x, z) plane with the dispersion falling off much more slowly along the z axis. We also plot the velocity ellipses in

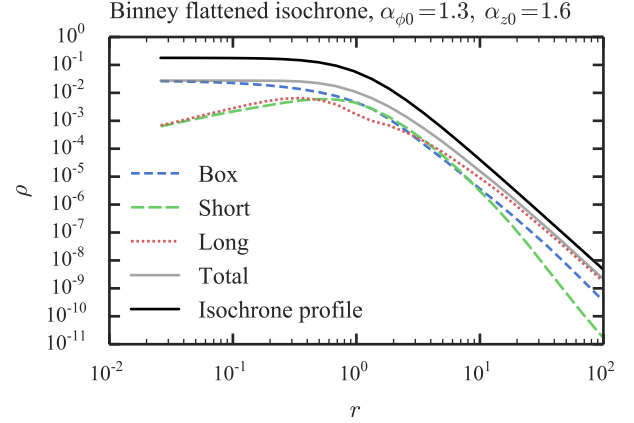


Figure 6. Contributions to the density in the triaxial Binney (2014) isochrone model along a radial line with $\phi = \frac{\pi}{4}$, $\theta = \frac{\pi}{4}$. Also shown is an isochrone profile offset by a factor of three for visibility. The positions are in units of r_0 and the density is in units of M/r_0 .

the same two planes. Clearly the velocity ellipses are very radial in both planes. The structure of the radial alignment in both planes is similar to the Hernquist case with the largest deviation from radial alignment occurring at $x = 0$ and small y and z .

4 APPLICATIONS OF MODELS

We present two applications of our new triaxial models.

4.1 Isophote twisting

One of the main lines of evidence for the triaxiality of some elliptical galaxies is the observation of isophote twisting (Bertola 1981; Emsellem et al. 2007). Isophote twisting is the change in the position angle of the major axis of the isophotal contours. In fast rotating galaxies or bulges (e.g., Stark 1977), this could be attributed to an inner bar/disc structure, whereas in slow rotators, the phenomenon is often attributed to triaxiality (e.g. Williams & Schwarzschild 1979). The projection of a triaxial model with ellipsoidal axis ratios varying with distance from the centre naturally produces gradual isophotal twists. Another explanation for the isophote twisting is an intrinsic twisting possibly due to a recent interaction. Several authors have studied the statistics of isophote twisting of large samples of galaxies (Carter 1978; Benacchio & Galletta 1980; Leach 1981). Fasano & Bonoli (1989) analysed a sample of galaxies and concluded that tidal interactions only played a small role in isophote twisting but that many of the galaxies studied had evidence of a central spheroid.

Irrespective of the exact origin of isophote twisting, the range of models able to reproduce this phenomenon is poor. The occurrence of isophotal twists was one of the main motivations for development of triaxial Stäckel models. So, it was a surprise when Franx (1988) showed that these models – unusually for triaxial systems – do not produce isophote twisting at any viewing angle. Therefore, we have hitherto been limited to constructing fully numerical (Schwarzschild or M2M) models to explore this phenomenon.

Here, we demonstrate that the model explored in Section 3.1.1

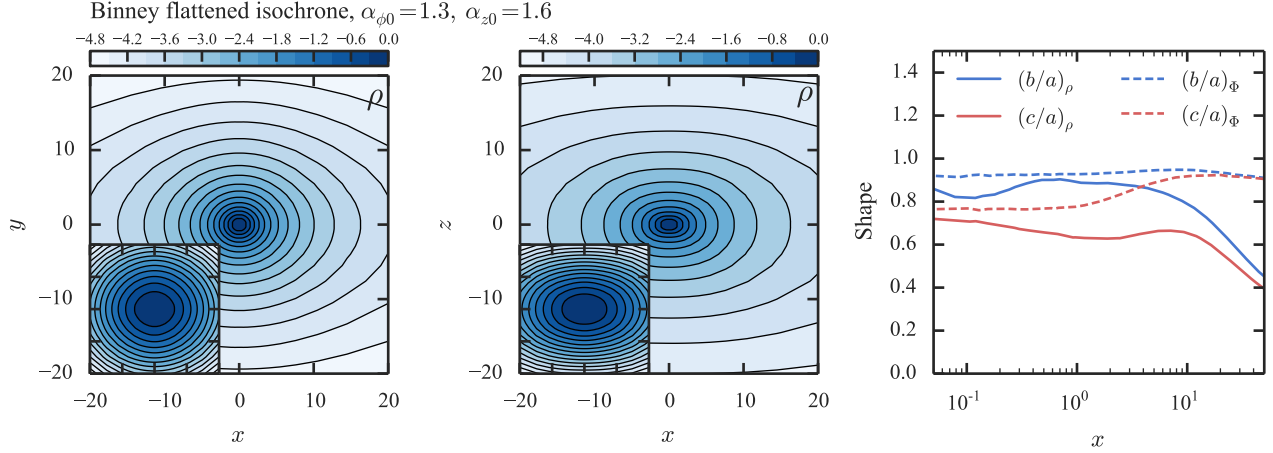


Figure 5. Density and shape of triaxial Binney isochrone model: the left panel shows a slice of the density in the (x, y) plane and the middle panel shows the equivalent in the (x, z) plane. The blue colours indicate the base 10 logarithm of the density relative to the central value. The insets show zoom-ins for $|x| < 1, y < |1|$ and $|x| < 1, |z| < 1$. In the right-hand panel we show the axis ratios of the fitted ellipses in these two planes with solid lines $[b/a]$ corresponding to (x, y) and c/a (x, z) . The dashed lines show the equivalent for the potential. The positions are in units of r_0 and the density in units of M/r_0^3 .

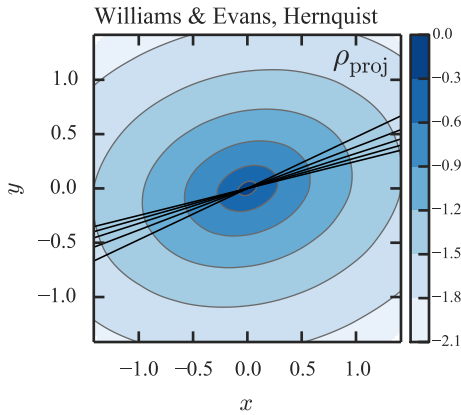


Figure 8. Logarithmic projected density of triaxial WEH model: the model is viewed along a unit vector with spherical polar angles $(\phi, \theta) = (\frac{\pi}{4}, \frac{\pi}{4})$. The lines show the major axis of ellipses fitted to the four innermost contours to indicate the clockwise twisting of the density contours as we move outwards. The positions are in units of r_0 and the unit of density is M/r_0^3 .

exhibits isophote twisting. In Figure 8, we show the projected density for the triaxial WEH model analysed in Section 3.1.1 when observed along a unit vector at spherical polar angles $(\phi, \theta) = (\frac{\pi}{4}, \frac{\pi}{4})$. We also show the major axes of ellipses fitted to the four innermost density contours. Clearly, the major axis of the density contours twists clockwise as we move out from the centre. The gradient of the twist is $\approx 8^\circ/r_0$. Recalling that the effective radius of a Hernquist model is $\approx 1.8r_0$, then the isophotal twisting gradient is $\approx 14^\circ/\text{effective radius}$, which is very comparable to the data (see e.g., Figure 8 of Leach 1981)

4.2 Radially unstable models

The radial orbit instability has received much attention in the literature from both theoretical and numerical studies (see Merritt (1999) for a nice review). The underlying physics is that when spherical models contain a high fraction of radial orbits, the models are unstable and tend to collapse to triaxial distributions. Polyachenko & Shukhman (2015) present a discussion of the mechanism by which the instability operates. Some systems are unstable to fast-growing even and odd tangential Jeans instabilities due to the lack of tangential kinetic energy. Other systems, which have more centrally concentrated radial orbits, are unstable to slow-growing bar-like modes of the type described by Lynden-Bell (1979) that act to align orbits. However, determining exactly when the instability will set in has been difficult to assess. Numerical experiments require the construction of N -body realizations so are limited to specific analytic equilibria such as Osipkov-Merritt $f(Q)$ models (Merritt & Aguilar 1985; Dejonghe & Merritt 1988; Meza & Zamorano 1997; Perez et al. 1996) or polytropes $f \propto (-E)^p L^q$ (Barnes et al. 1986), or use models constructed via Schwarzschild’s method. Recently, Antonini et al. (2009) and Vasiliev & Athanassoula (2012) have showed that triaxial models constructed via the Schwarzschild method are also susceptible to a radial-orbit instability when the central anisotropy of a Dehnen model with an inner density slope of 1 rises to $\beta \approx 0.4$. Theoretical studies have inspected the growing modes using the matrix method of Kalnajs (1977). Palmer & Papaloizou (1987) showed that all radially-anisotropic polytropes were unstable, whilst Saha (1991, 1992) and Weinberg (1991) derived conditions under which $f(Q)$ models were radially unstable. The conclusions from both approaches do not present a uniform picture and it seems difficult to predict exactly when a model is unstable without significant computation. Our new approach, however, provides another more general way to construct models that could be used to shed more light on the instability.

The degree to which the radial orbit instability is important in the landscape of galactic formation and evolution today is unclear. Some galaxies are believed to be weakly triaxial but the accretion

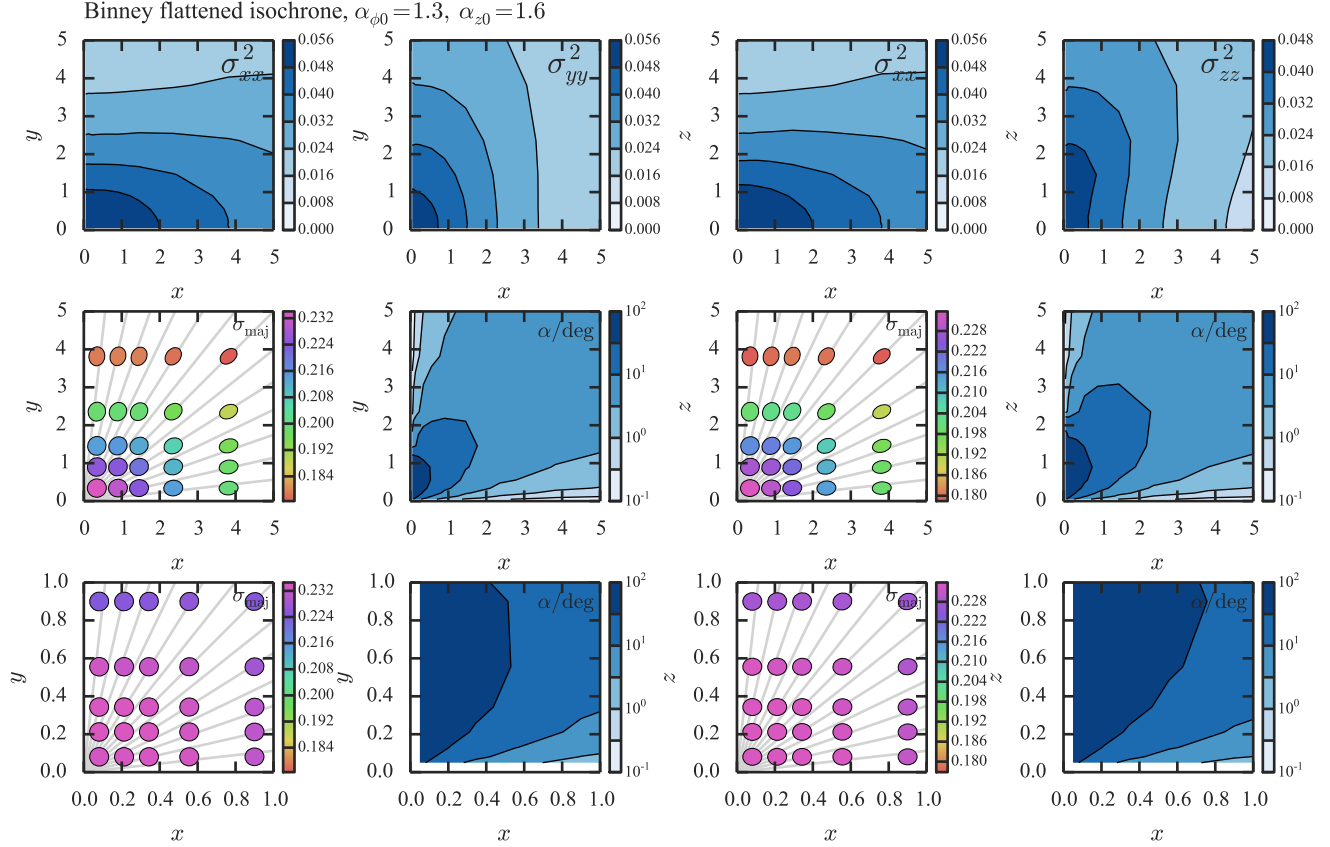


Figure 7. Velocity dispersions and ellipses of triaxial Binney isochrone model: in the top row, the first panel shows σ_{xx}^2 in the (x, y) plane, the second panel shows σ_{yy}^2 in the (x, y) plane, the third panel shows σ_{xx}^2 in the (x, z) plane and the fourth panel shows σ_{zz}^2 in the (x, z) plane. In the second row, the first panel shows the velocity ellipses in the (x, y) plane, the second panel shows the tilt with respect to the radial direction (drawn in light grey in the first panel) in the (x, y) plane, the third panel shows the velocity ellipses in the (x, z) plane and the fourth panel shows the tilt with respect to the radial in the (x, z) plane. The colours show the magnitude of the velocity dispersion along the major axis of each ellipse and only the shape of the ellipse is important. The sizes of the ellipses are arbitrary. The bottom row shows a zoom-in of the second row. The positions are in units of r_0 and the dispersions are in units of $\sqrt{GM/r_0}$.

of baryons and formation of black holes may decrease the degree of triaxiality at the centre of galaxies. Therefore, it is conceivable that the radial orbit instability may be mainly of theoretical interest and is often damped away in realistic systems. However, in the hierarchical picture of galaxy formation a galaxy grows through the accretion of smaller satellites which can be on very eccentric radial orbits. Therefore, a typical anisotropy profile is isotropic at the centre tending towards radial in the outskirts. It is therefore conceivable that the radial orbit instability sets in during the evolution and so is one of the mechanisms controlling the shape of galaxies.

We limit ourselves to models where $|J_\phi|$ and $|J_\theta|$ are on an equal footing ($q_z = 1$ in equation (16)). These should produce spherical models as they only depend on J_r and L . However, we allow a transition to triaxiality where the actions take on a slightly different meaning such that the models are not necessarily spherical. We construct WEH models with varying outer anisotropy by adjusting the parameter D_1 . All other parameters are as given in Williams & Evans (2015) isotropic Hernquist model, but T_1 is adjusted according to equation (18). In Figure 9, we show the anisotropy profiles for seven models restricting the models to spherical symmetry. We show the density contours and density and potential shapes in Figure 10 of four of these models that have been given the freedom to relax to triaxiality. We see that the

$D_1 = 0.4684$ model is spherical. $D_1 = 0.2$ has a triaxial structure in the outskirts of the density profile but the potential contours remain approximately spherical. For $D_1 = 0.114$, the model has developed a strong prolate shape in the outskirts and the potential contours are prolate throughout the explored volume. When D_1 is reduced further to 0.05, the contours become more strongly prolate. In the lower panel of Figure 9, we show the $(b/a)_\phi$ shape at $r = r_0$, $r = 10r_0$ and $r = 50r_0$ against D_1 . We see that beyond $D_1 = 0.2$ the models become prolate in nature. The anisotropy profile of the spherical equivalent of the critical $D_1 = 0.2$ model is shown in red in Figure 9.

It appears that when $D_1 \gtrsim 0.2$ the models remain approximately spherical, whereas for $D_1 \lesssim 0.2$ the models begin relaxing to a prolate shape. This threshold corresponds to an anisotropy at the scale radius of $\beta(r_0) \approx 0.25$. We interpret this result as follows: for $D_1 \lesssim 0.2$ the spherical models are unstable and susceptible to the radial orbit instability, such that the models relax to a radially-distended density distribution. As we have adiabatically relaxed the models, we are allowing instabilities that grow adiabatically slowly to persist. However, we have only allowed the models to transition through a range of triaxial models such that, although the models are radially unstable, it is not clear that they will relax to the given

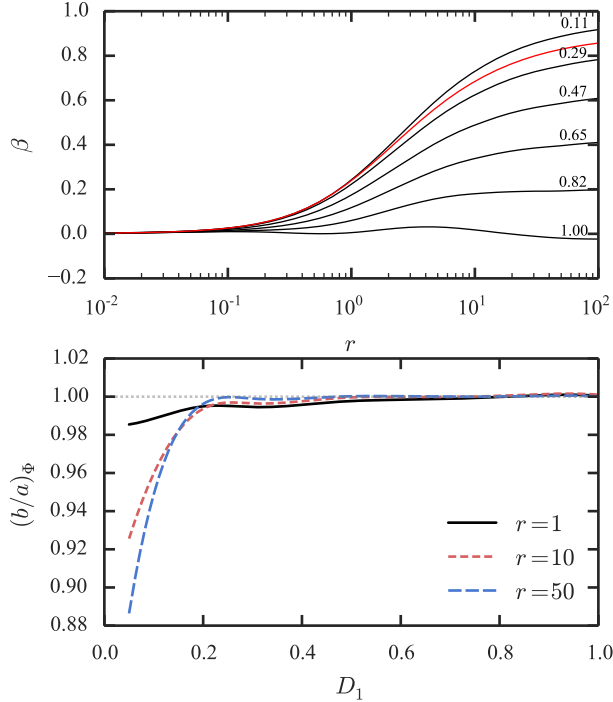


Figure 9. Radially unstable models: the top panel shows anisotropy profiles for seven spherical WEH models labelled by the parameter, D_1 , that controls the outer anisotropy. Spherical radius r is in units of r_0 . $D_1 = 1$ is the model presented in Williams & Evans (2015) and the other models use identical parameters apart from D_1 . The unlabelled red line corresponds to $D_1 = 0.2$, which is the critical model that separates the weakly spherical and triaxial endpoints. The bottom panel shows the shape of the potential contours in the (x, y) plane at three different major axis r values against D_1 for models allowed to relax to triaxiality.

distributions. It may be that other equilibria can be explored on the way to the final triaxial distribution.

In our approach the final models are approached via a series of triaxial non-self-consistent equilibria. However, in reality when $D_1 \lesssim 0.2$ the models will pass quickly through a series of non-equilibrium states to settle down to a final, possibly quite different, triaxial endpoint. Therefore, we conclude that $D_1 \approx 0.2$ is the transition point between stable and unstable spherical models, and that for $D_1 \approx 0.2$, we can find equilibrium models that are triaxial.

Antonini et al. (2009) and Vasiliev & Athanassoula (2012) found an approximate threshold for stability of triaxial Dehnen models constructed with the Schwarzschild method was $2T_r^2/T_t^2 \approx 1.4$ where T_r is the radial kinetic energy and T_t the tangential kinetic energy. Assuming a constant velocity anisotropy this threshold corresponds to $\beta \approx 0.3$ (approximately the critical anisotropy at the scale radius) so seems consistent with the result found here.

Our method involves the adiabatic relaxation of the models. Polyachenko & Shukhman (2015) have shown that some models are susceptible to fast-growing radial modes that grow on timescales of order the radial period of the responsible orbits and Antonini et al. (2009) present models that have modes that grow on times of ~ 20 crossing times. As our models are generated adiabatically, fast-growing modes may be suppressed.

5 DISCUSSION

The triaxial Stäckel models are exactly integrable and so possess no chaotic orbits. Our triaxial models are not integrable and will always contain some chaotic orbits, which are nonetheless assigned actions. In practice, the action label is meaningless and will vary with time. However, we have assigned the weight of this orbit based on the DF $f(J)$, so the weight should correspondingly change in time. However, it cannot, and so the model is not in equilibrium if it contains chaotic orbits.

Chaotic orbits appear regular on short times but slowly diffuse (Arnold diffusion). Arnold diffusion seems to be relatively slow compared to a Hubble time such that the equilibrium will be valid on scales of physical interest. However, at the centre of the models many of the orbits can diffuse very rapidly from one semi-regular orbit to the next such that the equilibrium is only valid on very short timescales (e.g., Valluri & Merritt 1998). Therefore, for our approach to hold good, we require the impact of chaotic orbits to be minimal otherwise the model will not be in true equilibrium.

In fact, all equilibrium construction approaches (including Schwarzschild or M2M) struggle to handle chaotic orbits. In the case of Schwarzschild modelling, one is limited to integrating all orbits for a fixed period of time such that a chaotic orbit can never fully be incorporated. Chaotic orbits have a single integral of motion, the energy, such that a model of solely the chaotic orbits can be constructed as $f_c(E)$. Merritt & Fridman (1996) adopt the approach of summing the densities of a series of chaotic orbits integrated for 100 dynamical times at each energy to construct this component. A full Schwarzschild model is then the combination of this chaotic piece plus an additional regular piece that can be included in the usual way. We could choose to follow the same procedure here by segregating chaotic orbits and constructing $f(J)$ models for the regular region of the phase-space. In this respect, our modelling approach does not seem inferior to other approaches and is probably equivalent.

Several authors have investigated the impact of chaotic orbits on numerically constructed Schwarzschild models. Voglis et al. (2002) and Capuzzo-Dolcetta et al. (2007) showed that, although non-rotating triaxial models contained 20 – 30 per cent of chaotic orbits by mass, only a few percent of these orbits by mass exhibited Arnold diffusion over a Hubble time. The impact of the chaotic orbits is a slow evolution of the axis ratios of the halos over time as corroborated by Zorzi & Muzzio (2012) and Vasiliev (2013a). However in contrast to this, Poon & Merritt (2002) have constructed models of triaxial nuclei with central black holes with considerable chaotic contributions which have fixed axis ratios over several dynamical times. When figure rotation is included the fraction of chaotic orbits by mass can increase significantly to ~ 50 per cent as shown by Voglis et al. (2006) and Manos & Athanassoula (2011). In conclusion although many orbits are formally chaotic in realistic non-rotating galactic potentials only a small fraction are chaotic on timescales of physical interest and these act to only weakly alter the shapes of the resulting models. Therefore, we conclude that the impact of chaos on the results presented in this paper is weak.

6 CONCLUSION

The range of triaxial equilibria for stellar systems remains largely uninvestigated. The variety of intrinsic shapes and anisotropies for which stable dynamical equilibria exist is not known, and the role

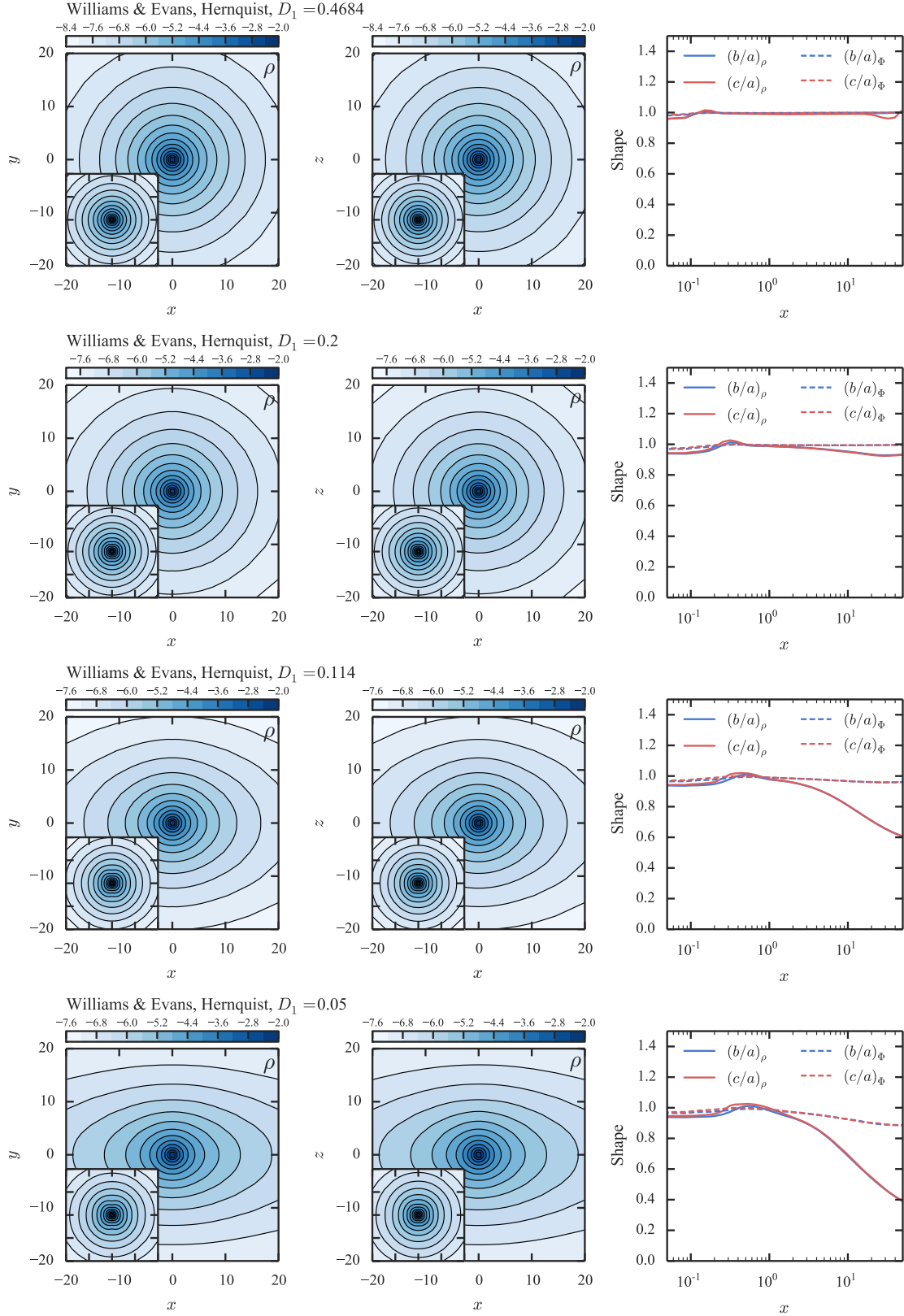


Figure 10. Range of triaxial WEH models with variable outer anisotropy. Each row shows the results for models of differing D_1 which is noted above each row. The left two panels in each row show density slices in the (x, y) and (x, z) planes with the insets showing zoom-ins of $|x| < 1$, $|y| < 1$ and $|x| < 1$, $|z| < 1$. The right panels show the axis ratios of ellipses fitted to the density and potential contours in these two planes [b/a corresponds to the (x, y) plane and c/a the (x, z) plane]. For $D_1 \gtrsim 0.2$ the models are spherical, whilst for $D_1 \lesssim 0.2$ the models collapse to triaxial distributions. The positions are in units of r_0 and the density in units of M/r_0^3 .

of figure rotation and tumbling is completely unexplored. One reason for this is the paucity of tools for building such models.

Much of our insight into triaxial equilibria comes from the Stäckel or separable potentials made famous by [de Zeeuw \(1985\)](#). Here, there are four orbital families, and self-consistent models can be built by orbit superposition or Schwarzschild's method ([Statler 1987](#)). There is strong evidence that the presence of four orbital families gives ample opportunity for exchanging orbits of different shapes, whilst keeping the total density unchanged ([Hunter & de Zeeuw 1992](#)). Therefore, the range of possible triaxial Stäckel equilibria may be very rich. Other than Stäckel models, there are only a handful of idealised triaxial equilibria in the literature ([Freeman 1966](#); [Vandervoort 1980](#)). Of course, Schwarzschild (1979) and made-to-measure ([Syer & Tremaine 1996](#)) techniques do in principle allow for a systematic exploration of triaxial equilibria. In practice, these techniques have been so far largely limited to axisymmetric systems because a smaller investment in computer time is required to sample phase-space in this case.

Here, we have developed a new way of studying triaxial systems. Many of the tools to do this exist in the literature, including algorithms for the swift calculation of actions ([Binney 2012](#); [Sanders & Binney 2015](#)) and possible ansatzes for forms of the distribution functions (DFs) in terms of the actions for both cored ([Binney 2014](#)) and cusped ([Williams & Evans 2015](#); [Posti et al. 2015](#)) galaxies. Synthesizing these results, we have shown how to build triaxial models with analytic DFs for the isochrone and Hernquist density laws. Their velocity ellipsoids are aligned with Cartesian coordinates near the centre, but spherical polar coordinates at large radii. In terms of orbital families, box orbits make a reasonable contribution at all radii in isochrone models, but they are less important at large radii in Hernquist models.

We have studied two particular features of the models. First, they can exhibit isophote twisting. This occurs when the position angle of the major axis of the isophotes changes with radius, with changes of the order of 10° over an effective radius being typical ([Leach 1981](#)). By projecting a triaxial Hernquist model built with a DF using the [Williams & Evans \(2015\)](#) ansatz, we demonstrated that our models could reproduce such a phenomenon. This is particularly valuable, as the Stäckel models – unusually for triaxial systems – do not exhibit isophote twisting ([Franx 1988](#)). Secondly, we used our models to explore the radial orbit instability. We considered the adiabatic relaxation of a family of DFs with central isotropy and variable outer anisotropy governed by a parameter D_1 . The endpoints of the relaxation may change from spherical to triaxial for some critical value of D_1 . Although the evolution is constrained, and so the endpoints may not be realised in practice, this nonetheless does give us the critical value at which the radial orbit instability sets in. We have given a particular example of this procedure for the triaxial Hernquist models.

There are some further directions and possible applications to pursue. The study of triaxial equilibria could be advanced by the combination of this work with N -body simulations or possibly made-to-measure models. As suggested in [Binney \(2014\)](#), these models can be used to create seeds for N -body simulations. These could then be evolved to investigate stability or the effects of growth of a disc or black hole in the model. It has been shown by [Antonini et al. \(2009\)](#) that equilibrium models constructed with Schwarzschild models can be dynamically unstable and it is expected that some models constructed via the method presented here will also be unstable. The only way to address this issue is through N -body modelling. Additionally, triaxiality seems an important effect to account for in the interpretation of observations on external

galaxies. To date only the Schwarzschild models of [van den Bosch et al. \(2008\)](#) have successfully modelled a triaxial elliptical galaxy. Therefore, one immediate application is to construct fits to ATLAS-3D data for slow rotators which may exhibit signatures of triaxiality. Finally, our models can be generalized to include streaming motion. The integrals of motion depend upon v_i^2 such that the sign of v_i is irrelevant. We are therefore able to give every particle a positive velocity such that the model has a net streaming velocity. Note that this would affect both the kinematical properties and the stability of the models constructed.

ACKNOWLEDGEMENTS

JLS acknowledges the support of the Science and Technology Facilities Council and thanks Angus Williams for useful conversations.

REFERENCES

- Aarseth S. J., Binney J., 1978, MNRAS, 185, 227
- Allgood B., Flores R. A., Primack J. R., Kravtsov A. V., Wechsler R. H., Faltenbacher A., Bullock J. S., 2006, MNRAS, 367, 1781
- Antonini F., Capuzzo-Dolcetta R., Merritt D., 2009, MNRAS, 399, 671
- Bailin J., Steinmetz M., 2005, ApJ, 627, 647
- Barnes J., Hut P., Goodman J., 1986, ApJ, 300, 112
- Barnes J. E., Hernquist L., 1996, ApJ, 471, 115
- Benacchio L., Galletta G., 1980, MNRAS, 193, 885
- Bertola F., 1981, in Structure and Evolution of Normal Galaxies, Fall S. M., Lynden-Bell D., eds., pp. 13–25
- Binney J., 1976, MNRAS, 177, 19
- Binney J., 1978, MNRAS, 183, 501
- Binney J., 1985, MNRAS, 212, 767
- Binney J., 2012, MNRAS, 426, 1324
- Binney J., 2014, MNRAS, 440, 787
- Binney J., Spergel D., 1984, MNRAS, 206, 159
- Binney J., Tremaine S., 2008, Galactic Dynamics: Second Edition. Princeton University Press
- Cappellari M. et al., 2007, MNRAS, 379, 418
- Cappellari M. et al., 2011, MNRAS, 413, 813
- Capuzzo-Dolcetta R., Leccese L., Merritt D., Vicari A., 2007, ApJ, 666, 165
- Carter D., 1978, MNRAS, 182, 797
- Davies R. L., Efstathiou G., Fall S. M., Illingworth G., Schechter P. L., 1983, ApJ, 266, 41
- de Zeeuw T., 1985, MNRAS, 216, 273
- Debattista V. P., Moore B., Quinn T., Kazantzidis S., Maas R., Mayer L., Read J., Stadel J., 2008, ApJ, 681, 1076
- Debattista V. P., Roškar R., Valluri M., Quinn T., Moore B., Wadsley J., 2013, MNRAS, 434, 2971
- Deg N., Widrow L., 2013, MNRAS, 428, 912
- Dehnen W., 2009, MNRAS, 395, 1079
- Dejonghe H., Merritt D., 1988, ApJ, 328, 93
- Dubinski J., 1994, ApJ, 431, 617
- Emsellem E. et al., 2011, MNRAS, 414, 888
- Emsellem E. et al., 2007, MNRAS, 379, 401
- Evans N. W., An J. H., 2006, Physical Review D, 73, 023524
- Evans N. W., de Zeeuw P. T., Lynden-Bell D., 1990, MNRAS, 244, 111
- Fasano G., Bonoli C., 1989, A & A, Supplement, 79, 291

- Franx M., 1988, MNRAS, 231, 285
- Franx M., Illingworth G., de Zeeuw T., 1991, ApJ, 383, 112
- Freeman K. C., 1966, MNRAS, 134, 1
- Galassi M., Davies J., Theiler J., Gough B., Jungman G., 2009, GNU Scientific Library - Reference Manual, Third Edition, for GSL Version 1.12 (3. ed.). Network Theory Ltd, pp. 1–573
- Häfner R., Evans N. W., Dehnen W., Binney J., 2000, MNRAS, 314, 433
- Hahn T., 2005, Computer Physics Communications, 168, 78
- Hénon M., 1960, Annales d’Astrophysique, 23, 474
- Hernquist L., 1990, ApJ, 356, 359
- Hunter C., de Zeeuw P. T., 1992, ApJ, 389, 79
- Illingworth G., 1977, ApJL, 218, L43
- Jing Y. P., Suto Y., 2002, ApJ, 574, 538
- Kalnajs A. J., 1977, ApJ, 212, 637
- Kazantzidis S., Kravtsov A. V., Zentner A. R., Allgood B., Nagai D., Moore B., 2004, ApJL, 611, L73
- Krajnović D. et al., 2011, MNRAS, 414, 2923
- Law D. R., Majewski S. R., 2010, ApJ, 714, 229
- Leach R., 1981, ApJ, 248, 485
- Long R. J., Mao S., Shen J., Wang Y., 2013, MNRAS, 428, 3478
- Lynden-Bell D., 1962, MNRAS, 124, 95
- Lynden-Bell D., 1979, MNRAS, 187, 101
- Manos T., Athanassoula E., 2011, MNRAS, 415, 629
- McGill C., Binney J., 1990, MNRAS, 244, 634
- Merritt D., 1985, AJ, 90, 1027
- Merritt D., 1999, Publications of the ASP, 111, 129
- Merritt D., Aguilar L. A., 1985, MNRAS, 217, 787
- Merritt D., Fridman T., 1996, ApJ, 460, 136
- Merritt D., Quinlan G. D., 1998, ApJ, 498, 625
- Meza A., Zamorano N., 1997, ApJ, 490, 136
- Ollongren A., 1962, Bulletin Astronomical Institute of the Netherlands, 16, 241
- Osipkov L. P., 1979, Pisma v Astronomicheskii Zhurnal, 5, 77
- Palmer P. L., Papaloizou J., 1987, MNRAS, 224, 1043
- Perez J., Alimi J.-M., Aly J.-J., Scholl H., 1996, MNRAS, 280, 700
- Polyachenko E. V., Shukhman I. G., 2015, MNRAS, 451, 5120
- Poon M. Y., Merritt D., 2002, ApJL, 568, L89
- Portail M., Wegg C., Gerhard O., Martinez-Valpuesta I., 2015, MNRAS, 448, 713
- Posti L., Binney J., Nipoti C., Ciotti L., 2015, MNRAS, 447, 3060
- Saha P., 1991, MNRAS, 248, 494
- Saha P., 1992, MNRAS, 254, 132
- Sanders J., 2012, MNRAS, 426, 128
- Sanders J. L., Binney J., 2014, MNRAS, 441, 3284
- Sanders J. L., Binney J., 2015, MNRAS, 447, 2479
- Schwarzschild M., 1979, ApJ, 232, 236
- Siopis C., Kandrup H. E., 2000, MNRAS, 319, 43
- Skokos C., Antonopoulos C., Bountis T. C., Vrahatis M. N., 2003, Progress of Theoretical Physics Supplement, 150, 439
- Stark A. A., 1977, ApJ, 213, 368
- Statler T. S., 1987, ApJ, 321, 113
- Syer D., Tremaine S., 1996, MNRAS, 282, 223
- Tremblay B., Merritt D., 1995, AJ, 110, 1039
- Udry S., 1993, A & A, 268, 35
- Valluri M., Merritt D., 1998, ApJ, 506, 686
- van den Bosch R. C. E., van de Ven G., Verolme E. K., Cappellari M., de Zeeuw P. T., 2008, MNRAS, 385, 647
- Vandervoort P. O., 1980, ApJ, 240, 478
- Vasiliev E., 2013a, MNRAS, 434, 3174
- Vasiliev E., 2013b, MNRAS, 434, 3174
- Vasiliev E., Athanassoula E., 2012, MNRAS, 419, 3268
- Vera-Ciro C., Helmi A., 2013, ApJL, 773, L4
- Voglis N., Kalapotharakos C., Stavropoulos I., 2002, MNRAS, 337, 619
- Voglis N., Stavropoulos I., Kalapotharakos C., 2006, MNRAS, 372, 901
- Wang Y., Mao S., Long R. J., Shen J., 2013, MNRAS, 435, 3437
- Weijmans A.-M. et al., 2014, MNRAS, 444, 3340
- Weinberg M. D., 1991, ApJ, 368, 66
- Williams A. A., Evans N. W., 2015, MNRAS, 448, 1360
- Williams A. A., Evans N. W., Bowden A. D., 2014, MNRAS, 442, 1405
- Williams T. B., Schwarzschild M., 1979, ApJ, 227, 56
- Zhao H., 1996, MNRAS, 283, 149
- Zorzi A. F., Muzzio J. C., 2012, MNRAS, 423, 1955
- Zotos E. E., 2014, A & A, 563, A19

APPENDIX A: CHOICE OF COORDINATE SYSTEM

In this appendix we detail how we choose the coordinate parameters α and β when using the Stäckel fudge algorithm of [Sanders & Binney \(2015\)](#). Given a general triaxial potential the only integral of motion we are in a position to calculate is the energy, E . Therefore, we choose to make the choice of α and β a function of E and we estimate the parameters using the closed loop orbits at each energy.

We construct a logarithmically spaced grid in energy from $E_0 = \Phi(0, y_{\min}, 0)$ to $E_1 = \Phi(0, y_{\max}, 0)$ with $N_E = 24$ grid points. We choose $y_{\min} = 0.015r_0$ and $y_{\max} = 180r_0$ where r_0 is the scale of the target model. To find the short-axis closed loop orbit at each energy we launch particles at a location y_i along the y -axis with velocity $v_{xi} = \sqrt{2E - 2\Phi(0, y_i, 0)}$ in the x -direction. We then record the y value of the next time the orbit crosses the y -axis ($y = y_f$) and the corresponding x -velocity v_{xf} . We repeat this procedure and minimise

$$\Omega_E^2(-y_i - y_f)^2 + (-v_{xi} - v_{xf})^2, \quad (\text{A1})$$

where Ω_E is the frequency of a circular orbit with energy E in a spherical potential with the radial profile corresponding to the profile along the x -axis in the triaxial potential. The same procedure is employed to find the long-axis loop orbits by replacing x with z in the above equations.

The long and short axis closed loop orbits are confined to the (y, z) and (x, y) planes respectively. In a Stäckel potential they follow elliptical lines of constant λ given by

$$\frac{y^2}{\lambda + \beta} + \frac{z^2}{\lambda + \gamma} = 1, \quad (\text{A2})$$

$$\frac{x^2}{\lambda + \alpha} + \frac{y^2}{\lambda + \beta} = 1.$$

With the closed orbits in a general potential found we can find the axis intercepts for the short axis loop: (x_s, y_s) and the long-axis loop (y_l, z_l) . Fitting ellipses to these points we find

$$\beta = \gamma - y_l^2 + z_l^2, \quad (\text{A3})$$

$$\alpha = \beta - x_s^2 + y_s^2.$$

In [Sanders & Binney \(2015\)](#) we performed this procedure by finding the closed loop orbits around the long and short axis and then minimising the variation in the action describing the circulation of the axis as a function of the coordinate parameters. This

procedure was unnecessary as, with the closed orbits, found the co-ordinate parameters can be simply calculated without finding the actions. The procedure presented here gives identical results to that employed in [Sanders & Binney \(2015\)](#) but is less cumbersome.

At some energies closed loop orbits cannot be found so we skip these points and fill them using a linear extrapolation. Additionally, we constrain $\alpha < \beta < \gamma$ such that x is the long axis and z the short axis. If our procedure produces estimates that violate this (e.g. in a near-spherical potential) we set $\alpha = \beta - r_0^2/10$ and $\beta = \gamma - r_0^2/20$, where r_0 is the scale-length of our models. Decreasing this arbitrary choice of $\gamma - \alpha$ and $\gamma - \beta$ does not significantly affect the accuracy of the calculations for radii $r < r_0$ but produces errors in the outskirts of the models ($r \gg r_0$) as the focal length is significantly smaller than the typical orbital scale. Our choice was selected such that the spherical isochrone and Hernquist models were reproduced.

APPENDIX B: MULTIPOLE EXPANSION

To find the potential from the density of an $f(\mathbf{J})$ model we use a multipole expansion. Here we give details of this approach. We evaluate the density on a 3D grid in spherical polar coordinates $(r, \phi, \cos \theta)$. The grid in radius r is logarithmically spaced between two radii r_{\min} and r_{\max} such that

$$r_i = a_0 e^{\delta_i} + r_{\min}, \quad (B1)$$

where

$$\delta_i = \frac{n_r}{N_r - 1} \log(r_{\max}/r_{\min}), \quad n_r = 0, 1, \dots, N_r - 1. \quad (B2)$$

The scale a_0 is chosen to be the scale radius of the model of interest, r_0 , and we set $r_{\min} = 0.01r_0$ and $r_{\max} = 200r_0$ which encloses 99 per cent of the total mass in both the spherical Hernquist and isochrone models. The $\cos \theta$ and ϕ grids are based on N_a -point Gauss-Legendre quadrature on the intervals $(-1, 0)$ and $(0, \pi/2)$ respectively. We set $N_r = 40$ and $N_a = 15$.

The potential Φ is expanded as

$$\Phi(r, \phi, \theta) = -4\pi G \sum_{l=0,2,\dots}^{l=l_{\max}} \sum_{m=0,2,\dots}^{m=l} \phi_{lm}(r) Y_l^m(\phi, \theta), \quad (B3)$$

where $Y_l^m(\phi, \theta)$ are spherical harmonics. The sum is over even values of l and m using a maximum l of $l_{\max} = 8$. We choose to work with a symmetric definition of $Y_l^m(\phi, \theta)$ ([Vasiliev 2013b](#)) given by

$$Y_l^m(\phi, \theta) = \frac{\mathcal{Y}}{\sqrt{2l+1}} \bar{P}_l^m(\cos \theta) \cos m\phi, \quad (B4)$$

where $\mathcal{Y} = \sqrt{2}$ if $m > 0$ otherwise $\mathcal{Y} = 1$. The normalized associated Legendre polynomials, $\bar{P}_l^m(\cos \theta)$, are calculated using the GNU Science Library (GSL, [Galassi et al. 2009](#)) as

$$\bar{P}_l^m(\cos \theta) = \sqrt{\frac{2l+1}{4\pi}} \sqrt{\frac{(l-m)!}{(l+m)!}} P_l^m(\cos \theta), \quad (B5)$$

where $P_l^m(\cos \theta)$ are the associated Legendre polynomials. The $Y_l^m(\phi, \theta)$ satisfy the orthogonality condition

$$\int_0^\pi d\theta \int_0^{2\pi} d\phi \sin \theta Y_l^m Y_{l'}^{m'} = \frac{\delta_{ll'} \delta_{mm'}}{2l+1}. \quad (B6)$$

$\phi_{lm}(r)$ is found by integrating the potential of the series of

spherical shells of thickness δr with mass $\rho_{lm}(r)\delta r$ inside and outside the radius r . Mathematically we have

$$\phi_{lm}(r) = r^{-l-1} I_{lm}^{(0)}(r) + r^l I_{lm}^{(\infty)}(r), \quad (B7)$$

where

$$I_{lm}^{(0)}(r) = \int_0^r da a^{l+2} \rho_{lm}(a), \quad (B8)$$

$$I_{lm}^{(\infty)}(r) = \int_r^\infty da a^{-l+1} \rho_{lm}(a),$$

and

$$\rho_{lm}(r) = 8(-1)^{m/2} \int_{-1}^0 d(\cos \theta) \int_0^{\pi/2} d\phi Y_l^m(\phi, \theta) \rho(r, \phi, \theta). \quad (B9)$$

The integral for $\phi_{lm}(r)$ is calculated using the trapezoidal rule in the coordinate $\delta = \log((r_i - r_{\min})/a_0)$ and the double integral for $\rho_{lm}(r)$ is found using Gauss-Legendre quadrature.

Similarly, to find the forces we must evaluate

$$\frac{\partial \phi_{lm}}{\partial r} = -\frac{l+1}{r^{l+2}} I_{lm}^{(0)}(r) + l r^{l-1} I_{lm}^{(\infty)}(r), \quad (B10)$$

and the derivatives with respect to ϕ and θ are found by analytically differentiating $Y_l^m(\phi, \theta)$.

We begin the calculation of these quantities by evaluating the density on the grid in (r, ϕ, θ) . This is the costliest part of the calculation but it can be parallelized. Then for each l and m we evaluate $\rho_{lm}(r)$ on the grid in r and use these results to compute $\phi_{lm}(r)$ and $\partial \phi_{lm}/\partial r$ on a grid in r , l and m . Assuming a finite mass model (i.e. $\rho_{lm}(r)$ has a shallower divergence than r^{-3} as $r \rightarrow 0$ and falls off steeper than r^{-3} as $r \rightarrow \infty$) the integral from $r = 0$ to $r = r_{\min}$ is found as $I_{lm}^{(0)}(r_{\min}) = \frac{1}{2} \rho_{lm}(r_{\min}) r_{\min}$. We set $I_{lm}^{(\infty)} = 0$ for $r > r_{\max}$.

For $r < r_{\min}$ we use quadratic extrapolation of $\phi_{lm}(r)$ and linear extrapolation of $\partial \phi_{lm}/\partial r$. For $r > r_{\max}$ we assume the density is zero and so extrapolate $\phi_{lm}(r)$ and $\partial \phi_{lm}/\partial r$ as

$$\phi_{lm}(r > r_{\max}) = \phi_{lm}(r_{\max}) \left(\frac{r_{\max}}{r} \right)^{l+1}, \quad (B11)$$

$$\frac{\partial \phi_{lm}}{\partial r}(r > r_{\max}) = \phi_{lm}(r_{\max}) \left(\frac{r_{\max}}{r} \right)^{l+2}.$$

The potential and forces calculation was tested using a triaxial perfect ellipsoid Stäckel potential ([de Zeeuw 1985](#)) as well as a flattened Hernquist model (replacing the square of the spherical radius r^2 with $m^2 = x^2 + (y/q_y)^2 + (z/q_z)^2$ in the Hernquist density profile) for which the potential and forces were calculated using equation (2.140) of [Binney & Tremaine \(2008\)](#) for the potential of a general density distribution stratified on concentric ellipsoids.

APPENDIX C: CROSS-CHECK WITH GENERATING FUNCTION APPROACH

In the main section of the paper we have used the triaxial Stäckel fudge approach of [Sanders & Binney \(2015\)](#) to construct the models due to its speed. However, the speed comes at the cost of increased errors in the actions. Using the Stäckel fudge the action estimates will oscillate. For some orbits this oscillation is genuine (see Section 5 on resonant and chaotic orbits), whilst for others it is a natural consequence of the approximation used. This naturally will introduce errors in the calculations to construct the models. [Sanders & Binney \(2015\)](#) explored this and discussed the error the

Stäckel fudge method produced when finding the moments of similar non-self-consistent models. It was found that the Jeans equation was satisfied to $\lesssim 10$ per cent for two tracer DFs in a triaxial NFW potential.

Sanders & Binney (2014) presented an alternate method for estimating actions in triaxial potentials. This algorithm will converge on the true action when one exists (for regular orbits), but is unfortunately much slower as it relies on orbit integration. However it can be used here as a cross-checking tool. Here we summarise the method and present a calculation of the density of one of our models using this approach.

C1 Generating function construction

The generating function method of Sanders & Binney (2014) is based on the construction of orbital tori methods pioneered by McGill & Binney (1990) and operates by construction of a generating function from the angle-actions in a simple analytic potential to those in the target potential from a series of orbit samples. Here we very briefly detail the method.

Given a target potential and a initial (x, v) coordinate we integrate the orbit. Here we choose to integrate for $T = 8t_{\text{orb}}$ where t_{orb} is the orbital period of a circular orbit with the same orbital energy in a spherical potential with a radial profile corresponding to the x -axis profile of the triaxial potential. From this orbit we sample $N_T = 200$ points and infer the orbital type (loop or box) from the angular momentum. We then choose a corresponding toy potential (triaxial harmonic oscillator for the box orbits and isochrone for the loops). We estimate the parameters of the toy potentials by fitting the toy forces to the true forces at the maximum $(|x|, |y|, |z|)$ points for the harmonic oscillator and by fitting the toy forces to the true forces at pericentre and apocentre for the isochrone potential (note this differs from the procedure employed in Sanders & Binney (2014) who minimised the variance of the toy Hamiltonian for the orbit samples). With the toy potential estimated we find the toy actions and angles (J', θ') . The true actions are then related to these toy variables via the generating function $S(\theta', J)$ as

$$J = J' - 2 \sum_{\mathbf{n}} \mathbf{n} S_{\mathbf{n}} \cos \mathbf{n} \cdot \theta', \quad (\text{C1})$$

where $S_{\mathbf{n}}$ are unknown Fourier components of the generating function. From our orbit samples we have N_T such equations which can be solved for $(J, S_{\mathbf{n}})$ by minimising the sum of the square differences between the toy actions and those calculated using the generating function series. We consider terms up to $|\mathbf{n}| \leq N_{\text{max}} = 6$. In addition to the checks of the solutions employed in Sanders & Binney (2014) to ensure good coverage of all modes, we also ensure the radial action for the loop orbits is positive, all actions for the box orbits are positive and the average of the action over the corresponding angle does not deviate from the estimated action by more than the maximum estimated action. If these criteria are not satisfied we increase the number of samples (if there is less than one sample per π phase of $\mathbf{n} \cdot \theta'$ for any mode \mathbf{n}) or the time integration window (if $\mathbf{n} \cdot \theta'$ does not wrap at least 2π for any mode \mathbf{n}) by a factor of two until an upper limit (four times the initial choice) and if the conditions are still not satisfied we return the average actions.

C2 A cross-check

Here we perform a cross-checking calculation for two of our models to measure the error the Stäckel fudge approach introduces. In

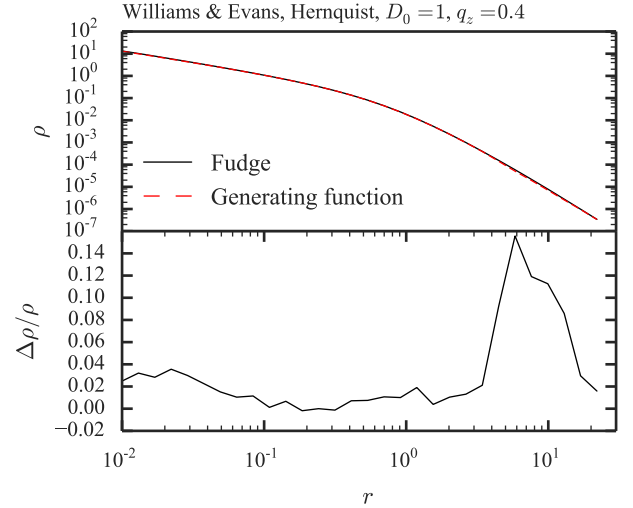


Figure C1. Density profile of triaxial WEH model along a ray with spherical polar angles $(\phi, \theta) = (\frac{\pi}{4}, \frac{\pi}{4})$ calculated using the triaxial Stäckel fudge method (black solid) and the generating function method (red dashed). The lower panel shows the relative difference in the density. The positions are in units of r_0 and the unit of density is M/r_0^3 .

Figure C1 we plot the density profile of the converged WEH model of Section 3.1.1 along a ray at spherical polar angle $(\phi = \frac{\pi}{4}, \theta = \frac{\pi}{4})$ calculated using the fudge method and the generating function method, and in Figure C2 we show the same calculation for the isochrone model of Section 3.2.1. Note the full convergence process was not performed using both approaches. We simply took the converged potential from the Stäckel fudge calculation and recalculated the density in this potential using the generating function approach. For the WEH model the relative error in the density is $\lesssim 10$ per cent everywhere. The largest errors occur outside $r \approx 5r_0$. For the isochrone model the relative error in the density is $\lesssim 2$ per cent for $r < 5r_0$ but the error steeply rises beyond this up to 30 per cent for $r = 20r_0$. It is unclear whether this systematic discrepancy is due to the fudge or generating function calculation but it appears to occur in the regions where the long-axis loop orbits are prominent so perhaps is due to their mishandling. We note that inspecting a less extremal model ($\alpha_\phi = 1.3, \alpha_z = 1.4$) we find that the two methods agree well.

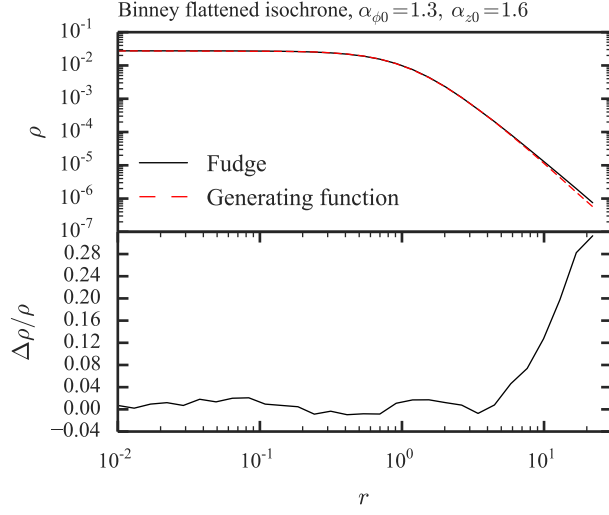


Figure C2. Density profile of triaxial isochrone model along a ray with spherical polar angles $(\phi, \theta) = (\frac{\pi}{4}, \frac{\pi}{4})$ calculated using the triaxial Stäckel fudge method (black solid) and the generating function method (red dashed). The lower panel shows the relative difference in the density. The positions are in units of r_0 and the unit of density is M/r_0^3 .